Supplemental Material

Journal of Climate

Influence of Atmospheric Circulation on Glacier Mass Balance in Western Tibet: An Analysis Based on Observations and Modeling

https://doi.org/10.1175/JCLI-D-20-0988.1

Supplemental Material

Influence of atmospheric circulation on glacier mass balance in western Tibet: an analysis based on observations and modeling

MEILIN ZHU

Key Laboratory of Tibetan Environment Changes and Land Surface Processes, Institute of Tibetan Plateau Research, Chinese Academy of Sciences, Beijing, China, and Byrd Polar and Climate Research Center, The Ohio State University, Columbus, Ohio, USA

LONNIE G. THOMPSON

Byrd Polar and Climate Research Center, The Ohio State University, Columbus, OH, USA

HUABIAO ZHAO, TANDONG YAO, and WEI YANG

Key Laboratory of Tibetan Environment Changes and Land Surface Processes, Institute of Tibetan Plateau Research, and Center for Excellence in Tibetan Plateau Earth Sciences, Chinese Academy of Sciences, Beijing, China

SHENGQIANG JIN

Key Laboratory of Tibetan Environment Changes and Land Surface Processes, Institute of Tibetan Plateau Research, Chinese Academy of Sciences, Beijing, China

Corresponding author:

Meilin Zhu, meilinzhu@itpcas.ac.cn

Lonnie G. Thompson, thompson.3@osu.edu

Contents of this file: Figures S1 to S9; Tables S1 to S4; Text S1

This supplemental material provides another nine figures, four tables and one text as seen in the main article.

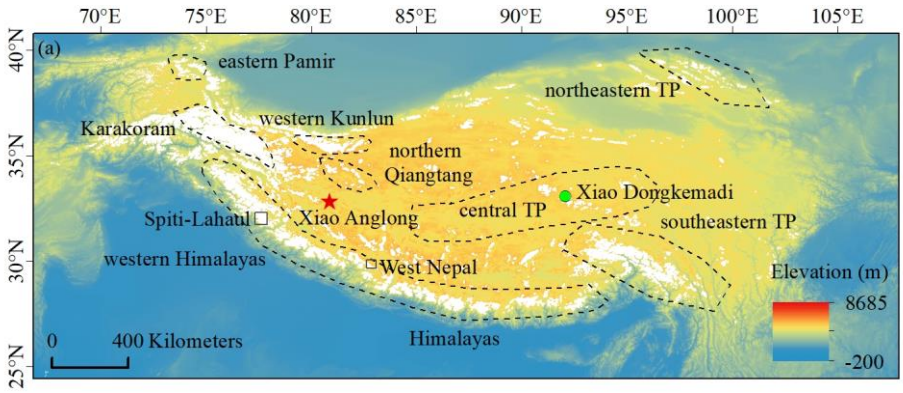

Figure S1. The locations of some glacierized areas (dashed outlines) on the Tibetan Plateau, the locations of two regional glaciers with geodetic mass balance measurements (squares) in the Himalayas, and the locations of Xiao Anglong (red star) and Xiao Dngkemadi (green point) glaciers. Glaciers are marked by white color.

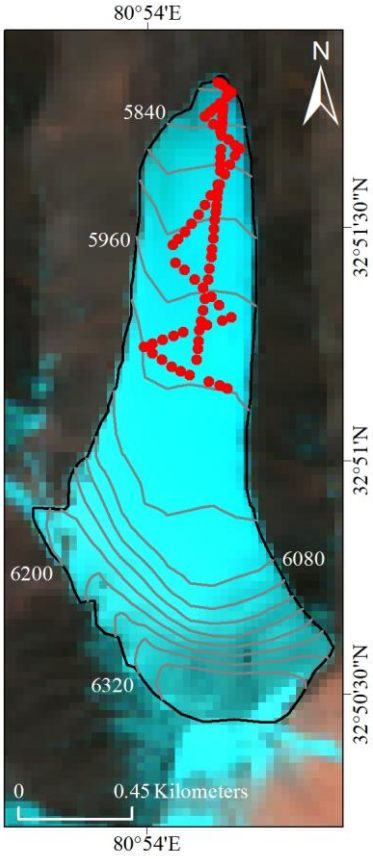

Figure S2. Repeat measurement points on Xiao Anglong Glacier from 2014 to 2018 using the Starfire E3050 or Starfire E3040 type DGPS. Red dots indicate the dGPS measurement locations. The maximum measured error in elevation changes from the Starfire E3050 or Starfire E3040 type DGPS should be less than 10 cm (Chen et al. 2019).

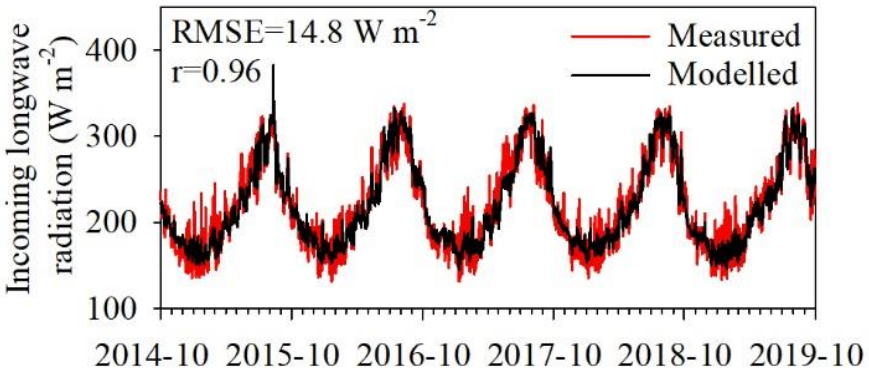

Figure S3. Modelled and measured daily mean incoming longwave radiation at AWS1. L_{in} is calculated using $L_{in} = \sigma(T_a + 273.15)^4((1-\tau_{atm}) + \tau_{atm} * (b_1 + b_2(\sqrt{e_a}))$. σ is the Stefan-Boltzmann constant (5.67×10^{-8} W m^{-2} K^{-4}); Bulk atmospheric transmissivity (τ_{atm}) is the ratio of the measured incoming shortwave radiation to the incoming shortwave radiation at the top of the atmosphere; e_a is the vapor pressure (hPa).

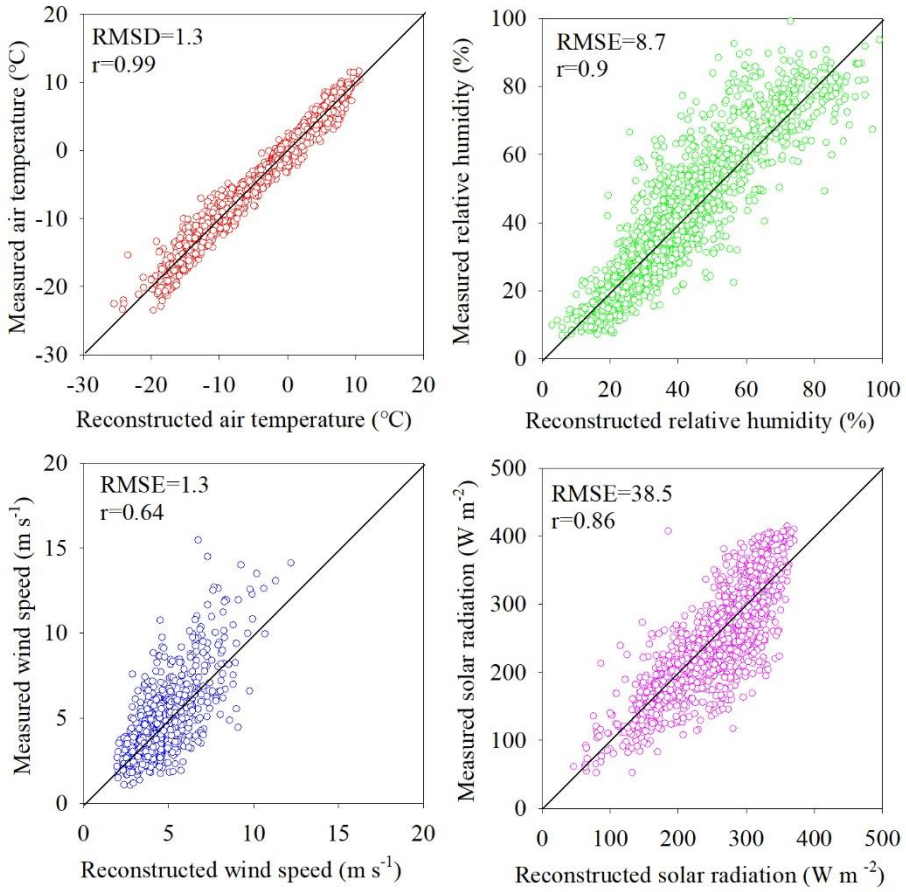

Figure S4. Comparisons of the reconstructed and observed meteorological variables.

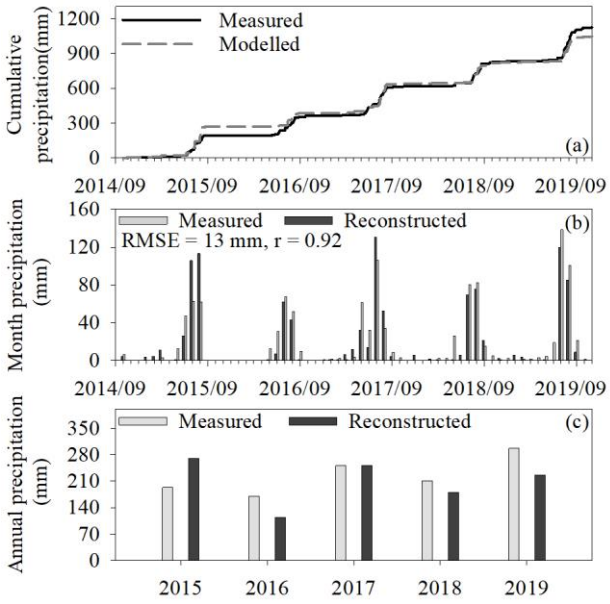

Figure S5. Comparison of (a) cumulative precipitation amount, (b) monthly precipitation and (c) annual precipitation between the T-200B precipitation gauge and the reconstructed precipitation data from Shiquanhe meteorological station during the observational period.

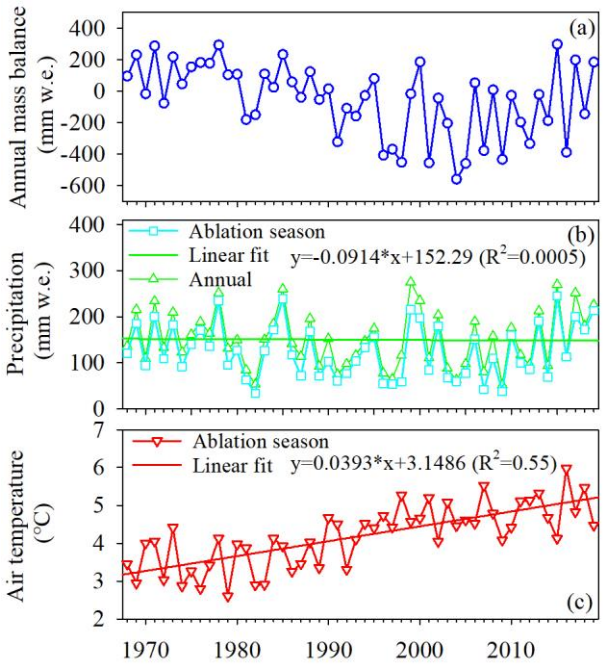

Figure S6. Temporal variation in the simulated annual mass balance for Xiao Anglong Glacier for 1968-2019 (a). Annual and ablation-season precipitation (b) and ablation-season air temperature (c) of the historical series and trends throughout 1968-2019 for Xiao Anglong Glacier. The year in the X axis indicates the balance year.

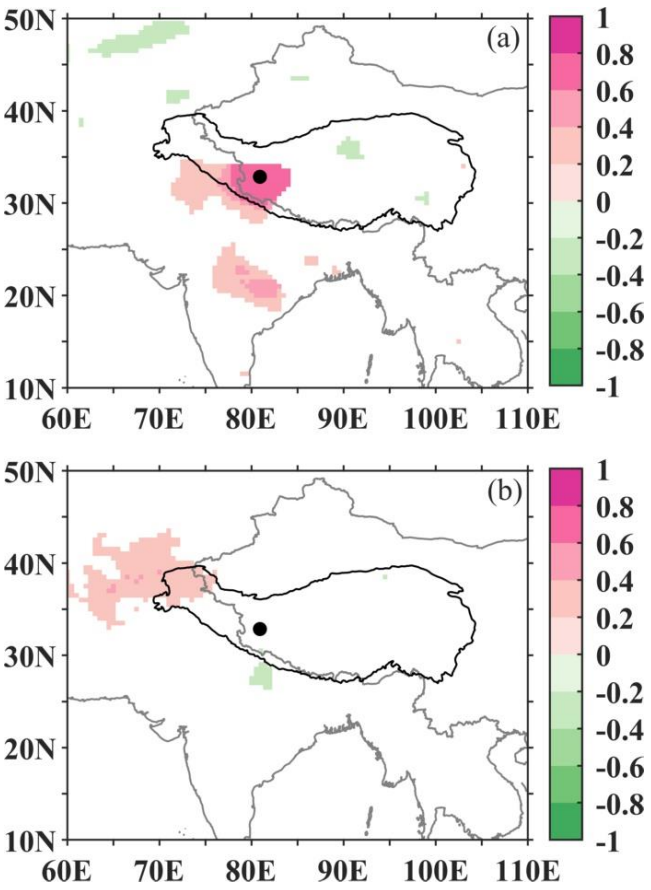

Figure S7. Spatial correlation patterns between the annual mass balance of Xiao Anglong Glacier and CRU gridded ablation-season precipitation (a), and between the annual mass balance of Xiao Anglong Glacier and CRU gridded ablation-season air temperature (b). On all figures, only correlations significant at the 95% confidence level are shown. The black line denotes the outline of the Tibetan Plateau. The black dot denotes the site of Xiao Anlgong Glacier.

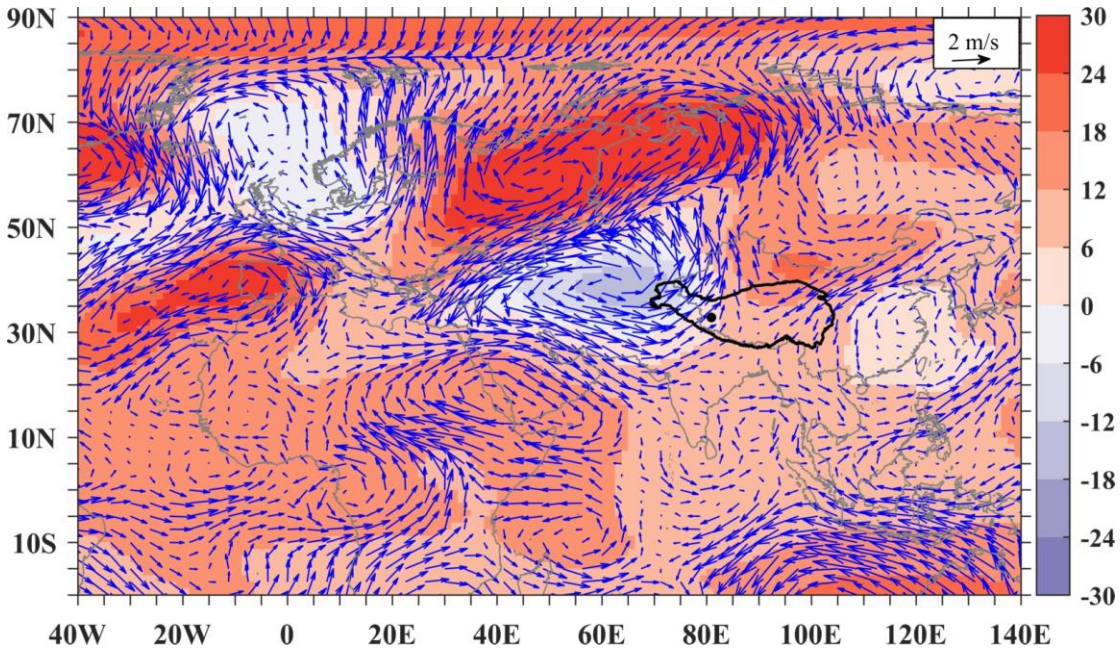

Figure S8. Differences in ablation-season geopotential heights (gpm) and wind fields at 300 hPa between the negative and positive mass balance phases for 1968-2019. Difference: negative mass balance phase values minus positive mass balance phase values. The black line denotes the outline of the Tibetan Plateau. The black dot points the location of Xiao Anglong Glacier.

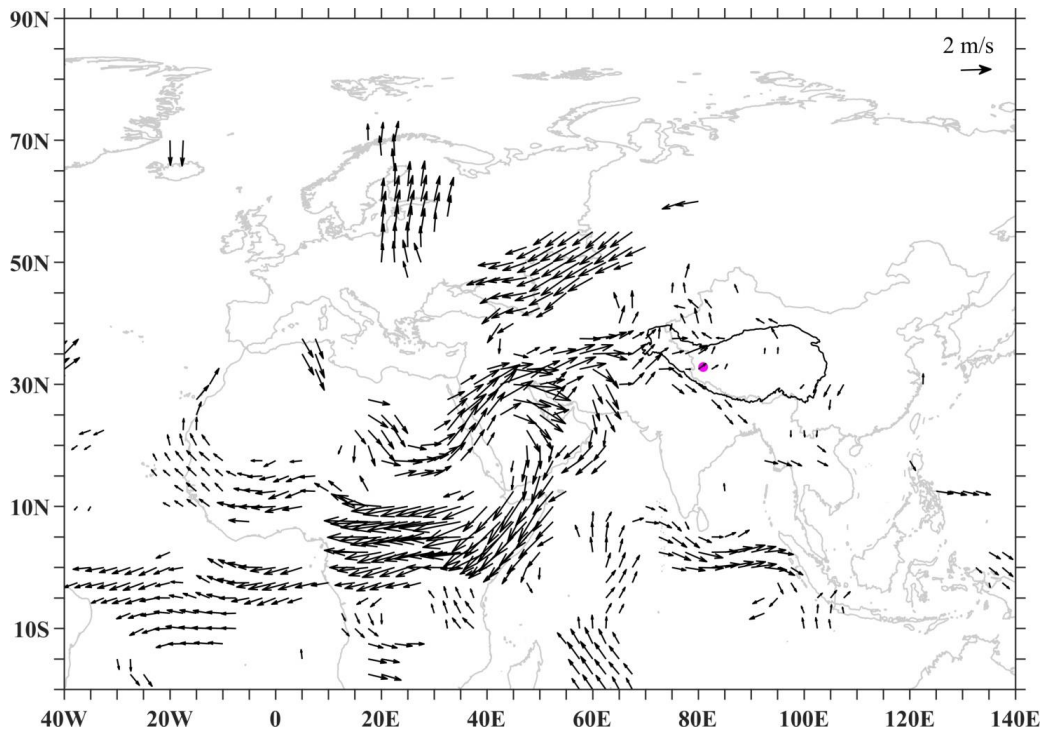

Figure S9. Differences in ablation-season 600 hPa wind speed fields between the negative and positive mass balance phases for 1968-2019. Difference: negative mass balance phase values minus positive mass balance phase values. The black line denotes the outline of the Tibetan Plateau. The pink dot points the location of Xiao Anglong Glacier. Only correlations significant at the 95% confidence level are shown.

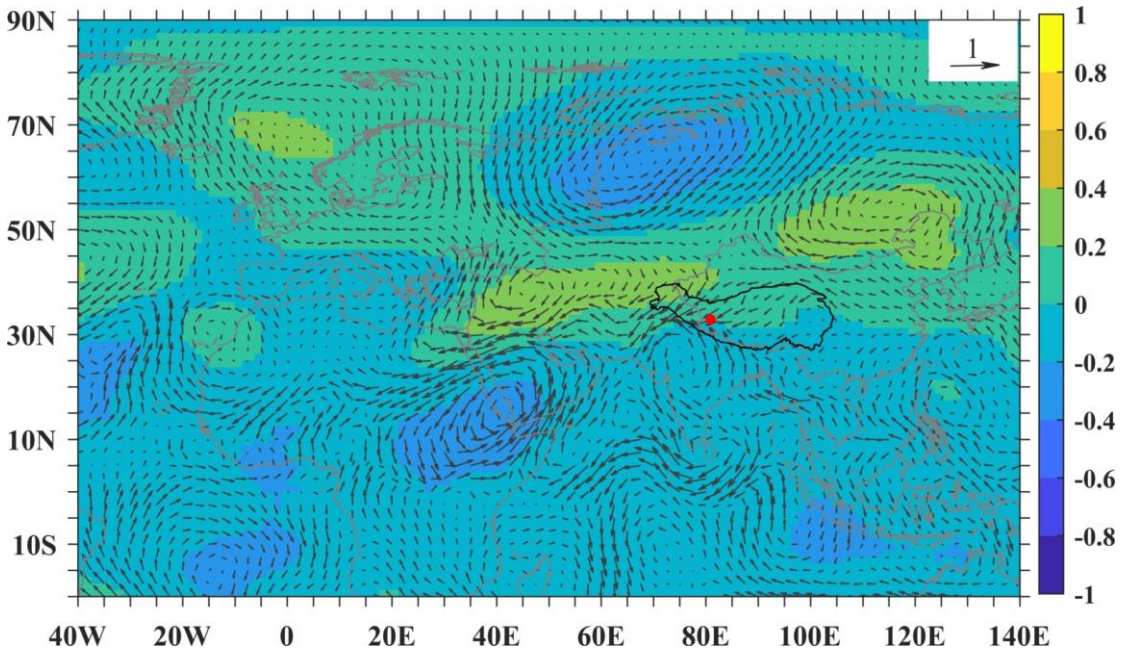

Figure S10. Correlation patterns between 500 hPa geopotential height fields/wind fields and region-averaged precipitation during the ablation season; Data are all detrended. The correlation length scale is shown in the upper right corner of panels. The 500 hPa geopotential heights and wind speed fields are from JRA55. The black line denotes the outline of the Tibetan Plateau. The red dot denotes the location of Xiao Anglong Glacier.

Table S1. Sensor information and technical specifications of two AWSs.

Parameters	Sensors	Accuracy	Height (m)
T_a	Vaisala HMP 45C	±0.2°C (-40 to +60°C)	3
RH	Vaisala HMP 45C	±2.5% (0-100%)	3
WS	Young 05103 wind monitor	±0.3 m/s	3
P	Geonor T-200B	±0.1 mm	1.5
S_{in}, S_{out}, L_{in} and L_{out}	Huxeflux NR01	1.8% (-40 to +80°C)	2.5
Press	Vaisala PTB210	± 0.35 hPa	2

T_a: air temperature (°C); *RH*: relative humidity (%); *WS*: wind speed (m s^{-1}); *P*: precipitation (mm); S_{in} and S_{out}: incoming and outgoing shortwave radiation (W m^{-2}); L_{in} and L_{out}: incoming and outgoing longwave radiation (W m^{-2}); *Press*: air pressure (hPa).

Table S2. Input parameters for the energy-based mass balance model.

Abbreviation	Parameter	Values
T_{rate1}	vertical air temperature gradient (ºC 100 m^{-1}) in the ablation season	-0.91
T_{rate2}	vertical air temperature gradient (ºC 100 m^{-1}) in the cold season	-0.75
P_{rate}	vertical precipitation gradient (% m^{-1})	0.115
RH_{rate1}	vertical relative humidity gradient in the ablation season (% 100 m^{-1})	0.9
RH_{rate2}	vertical relative humidity gradient in the cold season (% 100 m^{-1})	2.2
$S_{inrate1}$	Vertical solar radiation gradient in the ablation season (W m^{-2} m^{-1})	0.018
$S_{inrate2}$	vertical solar radiation gradient in the cold season (W m^{-2} m^{-1})	0.026
Z_{th}	snowfall event threshold (mm)	3.8
T_{snow}	phase threshold for snow (°C)	0
T_{rain}	phase threshold for rain (°C)	2
α_{snow}	fresh snow albedo	0.93
α_{firn}	firn albedo	0.53
ice_a	parameter for ice albedo	-0.0313
ice_b	parameter for ice albedo	0.2577
*t1** (day)	albedo time scale when surface temperature equal to 0	3.11
*t1** (day)	albedo time scale when surface temperature smaller than 0	6.11
*d** (cm)	albedo depth scale	8
b_1	parameter of L_{in}	0.436
b_2	parameter of L_{in} (hPa)	0.137
C_d	bulk coefficient of turbulent heat flux	0.002
ρ_{snow}	Fresh snow density (kg m^{-3})	100
ρ_{ice}	Ice density (kg m^{-3})	900

Table S3. Sensitivity of glacier-wide mass balance to parameters in the model.

Abbreviation	Parameter	Changes in parameters	Mass balance change (mm w.e. a^{-1})
a_{fresh}	fresh snow albedo	±10%	124
a_{firn}	firn albedo	±10%	115
*d**	albedo depth scale	±10%	10
*t1**	albedo time scale when surface temperature equal to 0	±10%	24
*t2**	albedo time scale when surface temperature smaller than 0		
ice_a	parameter for ice albedo	±10%	12
ice_b	parameter for ice albedo	±10%	14
T_{rain}	phase threshold for rain (°C)	±0.5ºC	4
T_{snow}	phase threshold for snow (°C)	±0.5ºC	2
Z_{th}	snowfall event threshold	±2 cm	10
C_d	Bulk coefficient for sensible and latent heat	±0.0018	62
P_{rate}	precipitation gradient	±10%	20

Table S4. The correlation coefficient among mass balance and air temperature and precipitation at different timescales.

	10	11	12	1	2	3	4	5	6	7	8	9
Annual mass balance and monthly mass balance	-0.16	-0.08	-0.2	0.21	0.23	0.13	0.1	0.18	**0.48**	**0.77**	**0.67**	-0.02
Annual mass balance and monthly T_a	0.15	-0.03	0.09	-0.03	-0.17	-0.28	0.01	0.07	-0.03	**-0.44**	**-0.37**	-0.03
Annual mass balance and monthly precipitation	-0.1	-0.06	-0.14	0.25	0.24	0.17	0.19	0.22	0.25	**0.69**	**0.52**	-0.06
Monthly mass balance and monthly T_a	-0.23	**-0.64**	**-0.59**	**-0.58**	**-0.69**	**-0.63**	-0.2	0.13	-0.14	**-0.62**	**-0.63**	**-0.37**
Monthly mass balance and monthly precipitation	**0.98**	**0.92**	**0.95**	**0.94**	**0.95**	**0.93**	**0.9**	**0.98**	**0.8**	**0.88**	**0.92**	**0.97**
Monthly precipitation and monthly T_a	-0.14	**-0.48**	**-0.43**	**-0.37**	**-0.58**	**-0.46**	0.01	0.26	0.24	**-0.49**	**-0.52**	**-0.39**

The bold indicate the p is less than 0.05.

Text S1:

Ablation-season precipitation was the main controlling factor for interannual variability in the mass balance, and both ablation-season precipitation and T_a play an important role in controlling interdecadal variability in the mass balance on Xiao Anglong Glacier. These phenomena may be linked to different strengths of climate variability between these two-time scales. The glacier mass changes caused by climate variability can be estimated by mass-balance sensitivity and strength of standard deviation of ablation-season T_a and annual (or ablation-season) precipitation on interannual and interdecadal time scales (Zhu et al. 2020). The standard deviation of the detrended ablation-season T_a on interannual time scales (0.54℃) was lower than that of ablation-season T_a on interdecadal time scales (0.78℃), because the warming trend over the last few decades was added on interdecadal scales. The standard deviation of the detrended ablation-season precipitation on interannual time scales (46.3%) was higher than that of ablation-season precipitation on interdecadal time scales (25.4%). Thus, the increased ablation-season T_a variability (or warming trend) and reduced ablation-season precipitation variability enhanced (or reduced) the influence of ablation-season T_a (precipitation) on changes in mass balance on interdecadal time scales when compared to interannual time scales.